

Supporting Information

Predictive approach to CVD of crystalline layers of TMDs: The case of MoS₂

Kranthi Kumar V.^a, Sukanya Dhar^a, Tanushree H. Choudhury^b, S. A. Shivashankar^a and

Srinivasan Raghavan^{a,b*}

^aCentre for Nano Science and Engineering, ^bMaterials Research Centre, Indian Institute of
Science, Bangalore – 560012, India.

* Corresponding author: sraghavan@cense.iisc.ernet.in

Methodology for thermodynamic analysis

The method¹ adjusts the moles of each species and finds the minimum Gibbs free energy consistent with mass balance conditions, assuming that equilibrium prevails in the process, which is applicable in CVD when the rate of deposition is low.²⁻⁴ Such thermodynamic calculations to predict MoS₂ growth by reaction of H₂S with MoCl₅⁵ and MoF₆⁶ has been attempted successfully previously. Thermodynamic analysis was also performed for deposition of Mo and Mo-compounds by PECVD from Mo(CO)₆ and MoF₆ as precursors and hydrogen or methane as reductants.⁷ However, to our knowledge, there has been no report exploring stability windows for CVD of MoS₂ from Mo(CO)₆ and H₂S by thermodynamic investigations, covering a wide range of gas ambient in particular. With this view, we have calculated the equilibrium molar concentrations of the films formed under various CVD conditions and gas ambient.

The approach requires identification of all possible reactants and reaction products. For the precursor Mo(CO)₆ in the presence of reacting gas H₂S, any product of the chemical reactions occurring during the CVD process should comprise one or more of the elements Mo, O, C, S and H. This would be true regardless of whether argon or hydrogen is used as the carrier gas, as argon is inert. Every possible solid product of the reactions involved was considered for the analytical study, which includes metallic molybdenum, its oxides, carbides, sulfides, carbon and sulfur. These are listed in Table S1, along with the possible gaseous products. Mass spectral analysis of Mo(CO)₆ has been consulted in choosing the gaseous compounds included in the modeling. The primary fragments indicated in mass spectral analysis can undergo collisions with the molecules of the reacting gas H₂S or atoms/molecules arising from it, and hydrogen (if used as in the carrier gas), leading to further fragmentation and reaction(s) to yield various gaseous products. Thermodynamic computations were performed, in a methodology described earlier^{4,8} using 100% Argon, 100% hydrogen, and argon/hydrogen mixtures of different compositions (Ar:H₂=25:75, 50:50, 75:25) as carrier gases, using a commercially available PC-based software program [Autokumpu HSC Chemistry 6.1, Finland]. Being an inert gas, argon does not take part in any chemical reaction, but its flow rate compared to those of precursor vapor, reacting gas, and hydrogen (when Ar/H₂ mixture is used as a carrier) affects the partial pressures of the gaseous species, thereby varying the compositions at equilibrium. The corresponding phase stability diagrams were also constructed.

Table S1. List of chemical species considered for the equilibrium calculation.

Condensed Phases	Mo, MoC, Mo ₂ C, Mo ₃ C ₂ , MoO ₂ , MoO _{2.75} , MoO _{2.875} , MoO _{2.889} , MoO ₃ , Mo ₄ O ₁₁ , MoO ₃ -H ₂ O, MoS ₂ , MoS ₃ , Mo ₂ S ₃ , Mo(CO) ₆ , C, S (rhombic), S (monoclinic).
Gaseous phases	CH ₄ , CO, CO ₂ , COOH, COS, CS, CS ₂ , H ₂ , HS, H ₂ S, H ₂ S ₂ , HCO, H ₂ CO, HCOOH, CH ₃ COCH ₃ , HCHO, CH ₃ CHO, H ₂ SO ₄ , S, S ₂ , S ₃ , S ₄ , S ₅ , S ₆ , S ₇ , S ₈ , SO, SO ₂ , SO ₃ , S ₂ O, O ₂ , H ₂ O, H ₂ O ₂ , Mo(CO) ₆ , Ar.

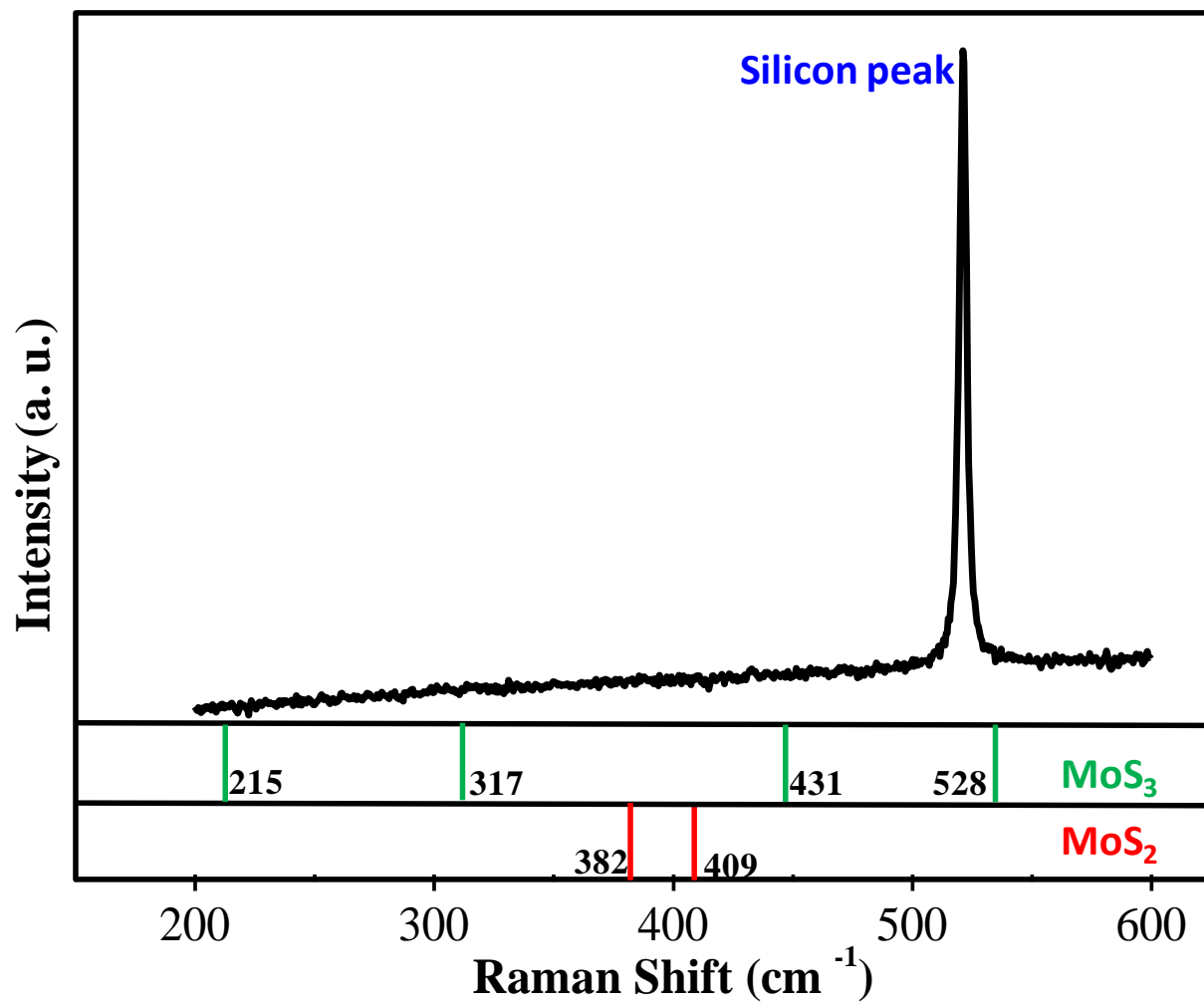


Fig. S1 Raman spectrum after deposition on SiO₂/Si substrate at 200°C. No evidence for MoS₂ and MoS₃ is seen in depositions at T<200°C.

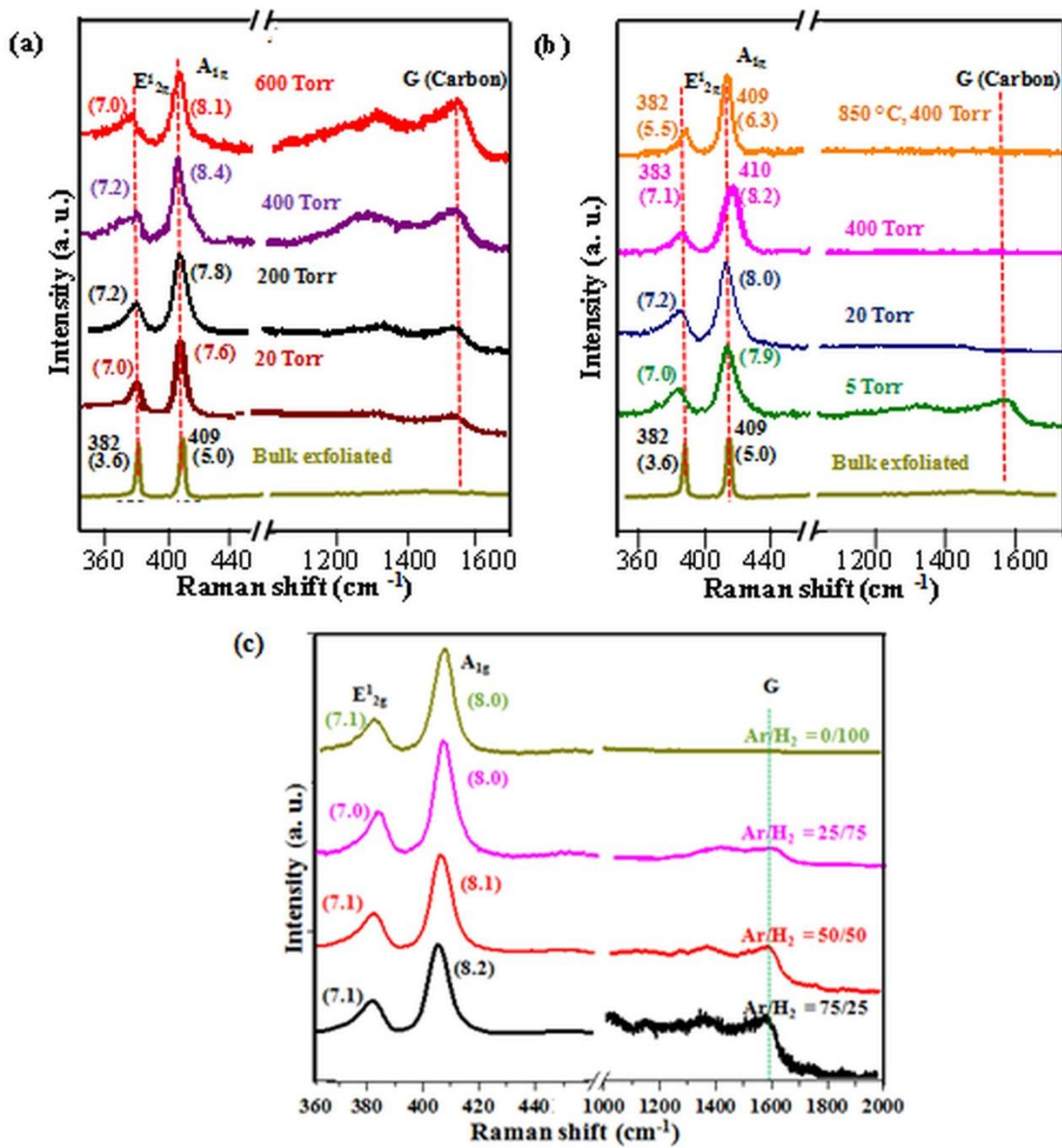


Fig. S2 Raman spectra along with their FWHM of samples deposited at 500°C (a) in argon ambient (b) in hydrogen ambient, as a function of increasing P_{tot} . Carbon content increases with P_{tot} in argon ambient, whereas it diminishes in hydrogen ambient. The Raman spectrum of the sample deposited in hydrogen ambient at 850°C is also shown in (b) for comparison. (c) when the Ar:H₂ ratio is varied at 20 Torr.

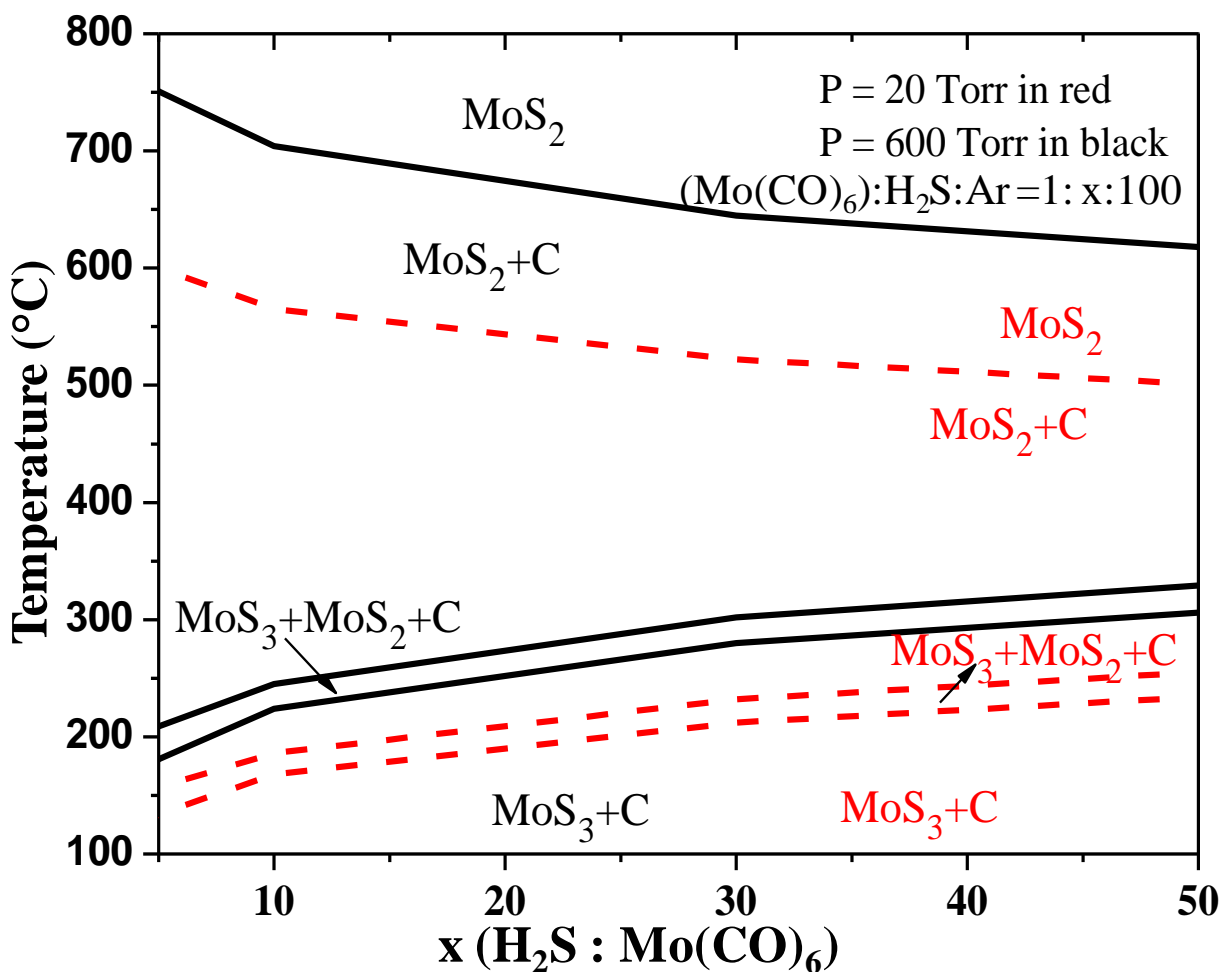


Fig. S3 CVD phase stability diagram for the formation of solid phases as a function of substrate temperature and x [molar flow rate ratio of H_2S and Mo(CO)_6] at 600 Torr. The red dotted lines represent the phase stability diagram at 20 Torr. The temperature window for the formation of pure MoS_2 is wider at $P_{\text{tot}} = 20$ Torr, and “opens” at a lower temperature than at 600 Torr.

Supersaturation calculation for kinetic control

The equation assumed for the thermodynamic modeling and supersaturation control is given in Equation 1.



The supersaturation for this reaction can be written as

$$\Delta G = \Delta G^\circ + RT \ln \left(\frac{\eta_{\text{Mo(CO)}_6} \eta_{\text{H}_2\text{S}}^2 \eta_{\text{tot}}^5}{\eta_{\text{CO}}^6 \eta_{\text{H}_2}^2 P_{\text{tot}}^5} \right)$$

Where, $\Delta G^\circ = -RT \ln K_{\text{Eq}}$

$$\text{Hence, } \Delta G = RT \ln \left(\frac{\eta_{\text{Mo(CO)}_6} \eta_{\text{H}_2\text{S}}^2 \eta_{\text{tot}}^5}{\eta_{\text{CO}}^6 \eta_{\text{H}_2}^2 P_{\text{tot}}^5 K_{\text{Eq}}} \right) \quad (2)$$

At 850°C, $\Delta G^\circ = 675 \text{ kJ/mol}$ and $K_{\text{Eq}} = 2.48 \times 10^{31}$.^{9,10} For a given flux, the effect of increasing pressure can be estimated as follows.

$$\text{At pressure, } P_{\text{tot},1}, \Delta G^1 = RT \ln \left(\frac{\eta}{P_{\text{tot},1} K_{\text{Eq}}} \right)$$

$$\text{At pressure, } P_{\text{tot},2}, \Delta G^2 = RT \ln \left(\frac{\eta}{P_{\text{tot},2} K_{\text{Eq}}} \right)$$

The difference in supersaturation on going from $P_{\text{tot},1}$ to $P_{\text{tot},2}$ is

$$\begin{aligned} \Delta G^1 - \Delta G^2 &= RT \ln \left(\frac{\eta}{P_{\text{tot},1}^5 K_{\text{Eq}}} \times \frac{P_{\text{tot},1}^5 K_{\text{Eq}}}{\eta} \right) \\ \Delta G^1 - \Delta G^2 &= RT \ln \left(\frac{P_{\text{tot},2}^5}{P_{\text{tot},1}^5} \right) \end{aligned} \quad (3)$$

For $P_{\text{tot},1} = 20 \text{ Torr}$ and $P_{\text{tot},2} = 850 \text{ Torr}$, the change in supersaturation as given by Equation 3 is 175 kJ/mol.

Table S2: Supersaturation calculated from Equation 2, along with the number of layers obtained

Run details: P _{tot} : flow rates of Mo(CO) ₆ :H ₂ S:carrier gas (sccm) at 850°C	Growth duration (seconds)	MoS ₂ characteristics Number of layers	Samples used for characterisation
20 Torr, 1: 10: 100	60	3L in all samples	3L for Electrical(Fig 6), XPS (Fig. 5), SEM Fig(3)
20 Torr, 1: 10: 50: 50 (Ar:H ₂)	60	4-3L in all samples	
20 Torr, 1: 10: 500: 500 (Ar:H ₂)	180	6,5,4L and 3L only in last 2 samples	
20 Torr, 1: 10: 1000 H ₂	180	5-3L	5,4L for Electrical(Fig. 6) , XPS (Fig 5.)
400 Torr, 1:10: 1000 H ₂	15	Almost connected round islands	
500 Torr, 1: 10: 1000 H ₂	60	1L	1L – TEM (Fig. 5)
500 Torr, 1: 10: 500: 500 (Ar:H ₂)	40	3-1L	
550 Torr, 1: 10: 1000	60	Islands from 3 rd sample	SEM (Fig. 3)
850 Torr, 1: 10: 1000	40	25 μ triangular islands	SEM, AFM (Fig. 3)

Mo(CO)₆ flow rate:

$$\frac{\eta_{Mo}}{P_{Mo}} = \frac{\eta_{Bubbler}}{P_{Bubbler}}$$

Carrier flow in the bubbler is 15 sccm with bubbler pressure at 20 psi (1035 Torr) and vapour pressure of Mo(CO)₆ is 124 Torr at 120°C

Hence, $\eta_{Mo} = 1.8$ sccm

H₂S flow rate: 18 sccm

Supersaturation calculation for MoS₂ growth by physical vapor transport of MoS₂

In case of physical vapor transport with MoS₂ powder¹¹ is maintained at 900 °C, while the growth occurs at 650 °C.

The reaction in this deposition that has been considered is



In this case the flux of MoS₂ vapors is the equilibrium partial pressure of MoS₂ at 900 °C.

The partial pressure can be calculated from the standard Gibbs free energy ΔG_{900}° as

$$\begin{aligned} \Delta G_{900}^\circ &= -RT \ln [P_{\text{MoS}_2}] \\ P_{\text{MoS}_2} &= \exp\left(-\frac{\Delta G^\circ}{RT}\right) \end{aligned} \quad (2)$$

$$\Delta G_{900}^\circ = 369 \text{ kJ/mol, hence, } P_{\text{MoS}_2} = 3.546 \times 10^{-17}$$

At the growth temperature of 650 °C, the supersaturation for Equation1 is as follows

$$\begin{aligned} \Delta G &= \Delta G_{650}^\circ + RT \ln(P_{\text{MoS}_2}) \\ \Delta G &= RT \ln(P_{\text{MoS}_2} / K_{\text{Eq}}) \end{aligned} \quad (3)$$

Using $\Delta G_{650}^\circ = 422 \text{ kJ/mol}$, Equation 3 gives superstation at 650 °C to be 131 kJ/mol.

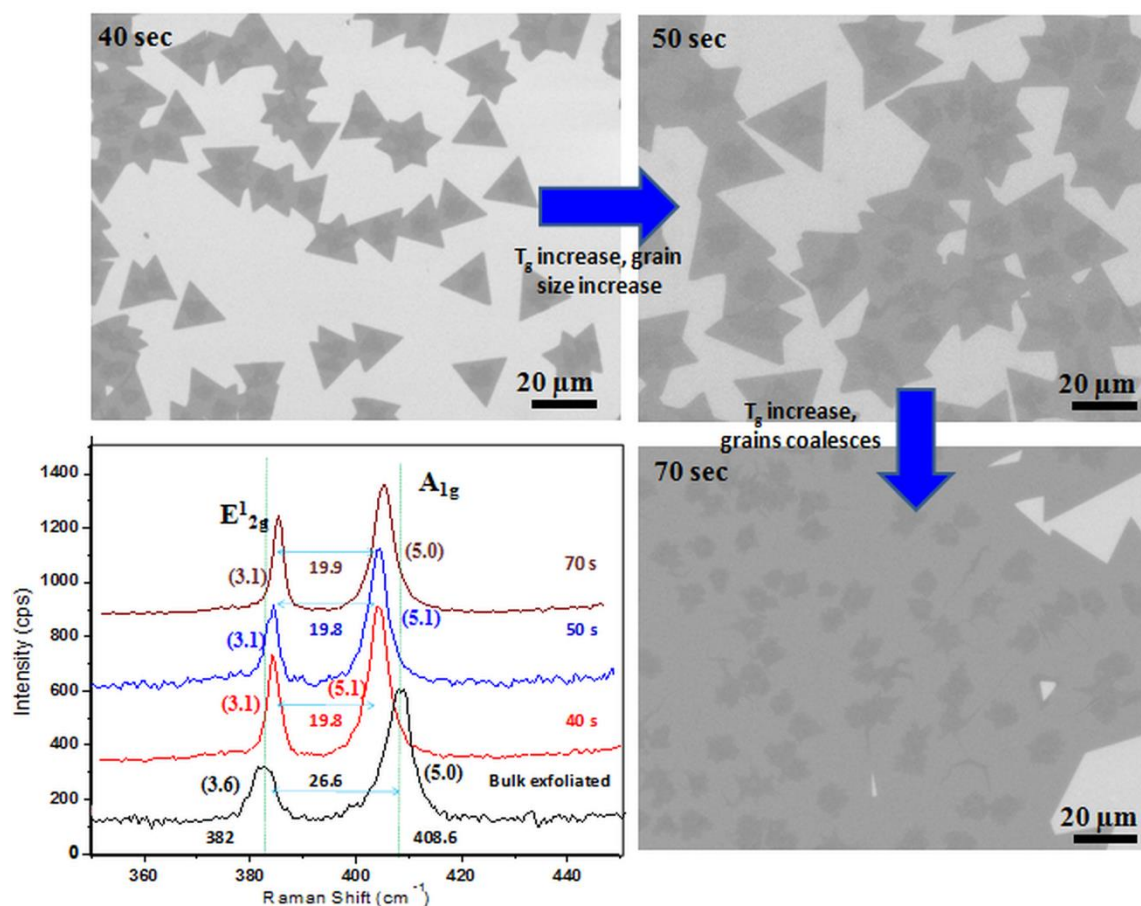


Fig. S4 Grain growth at 850°C, 850 torr at various growth time (T_g): (a) SEM image of triangular islands of MoS₂ single layers at growth time (T_g) of 40 s (b) SEM image at $T_g = 50$ s showing grain growth (c) SEM image at 70 s showing fully covered 1L MoS₂ (d) Raman plots at various growth times with bulk exfoliated as reference.

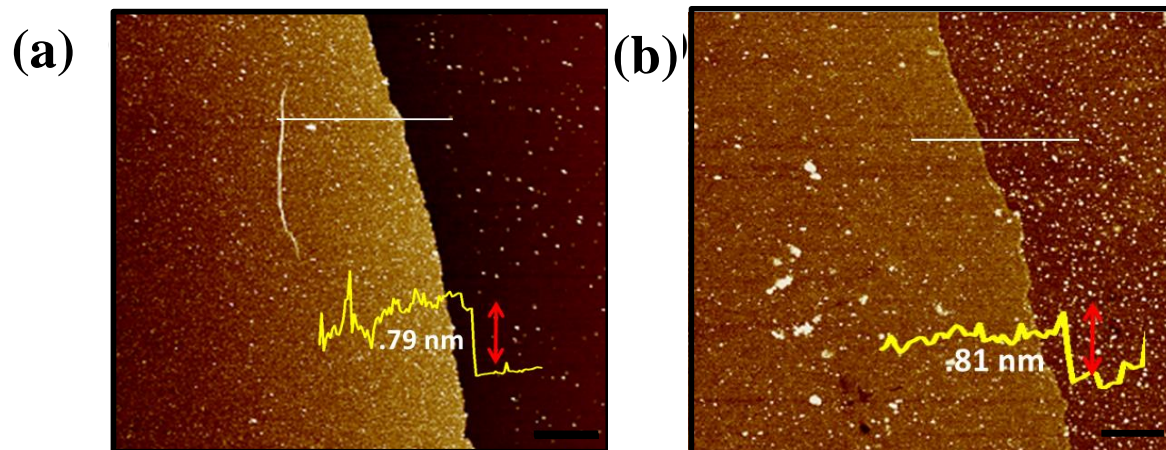


Fig. S5 AFM images of monolayers of MoS₂ grown on (a) SiO₂/Si and (b) Fused quartz.

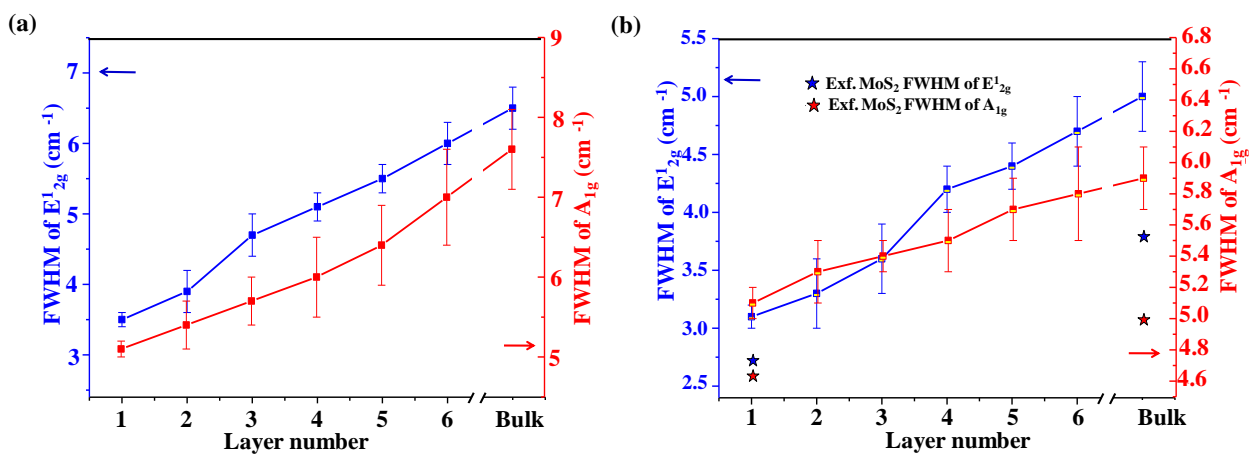


Fig. S6 (a) and (b) Shows variation in FWHM of E_{2g}^1 and A_{1g} peaks of Raman, plotted as function of layer thickness (a) without sulphurization (b) FWHM obtained when sulphurization is carried out and includes FWHM of exfoliated MoS_2 for reference.

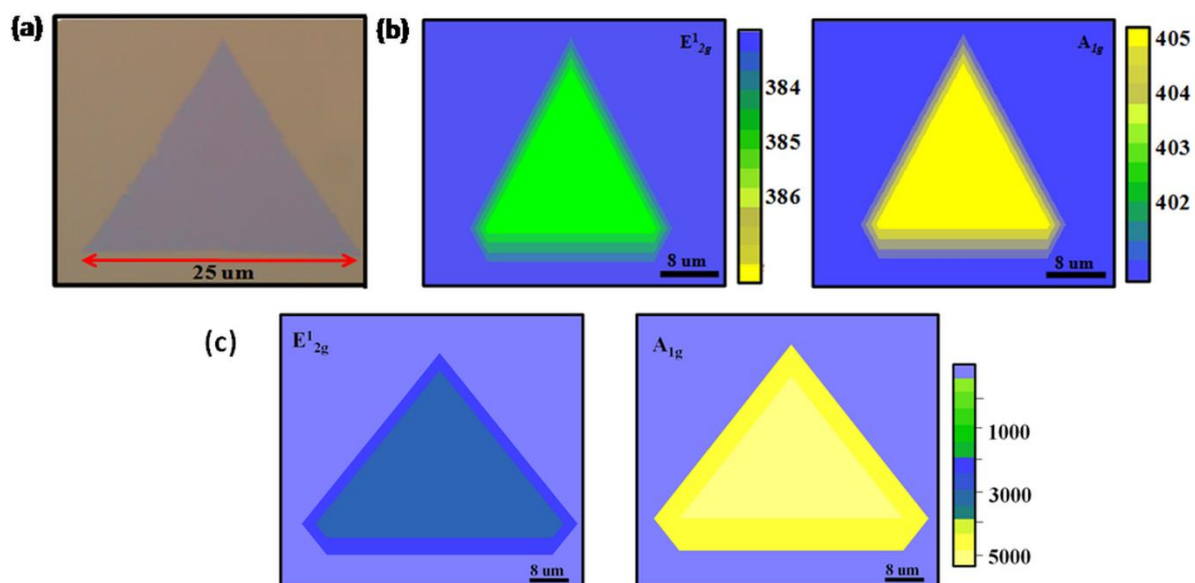


Fig. S7 Uniform – islands of monolayer MoS₂ (a) optical image of triangular single crystal MoS₂ (b) Raman mapping of (E_{12g}¹ peak and A_{1g} peak with respect to peak positions) of MoS₂ triangle showing uniformity of single layer. (c) Raman mapping of (E_{12g}¹ peak and A_{1g} peak with respect to intensity) MoS₂ triangle showing uniformity of single layer.

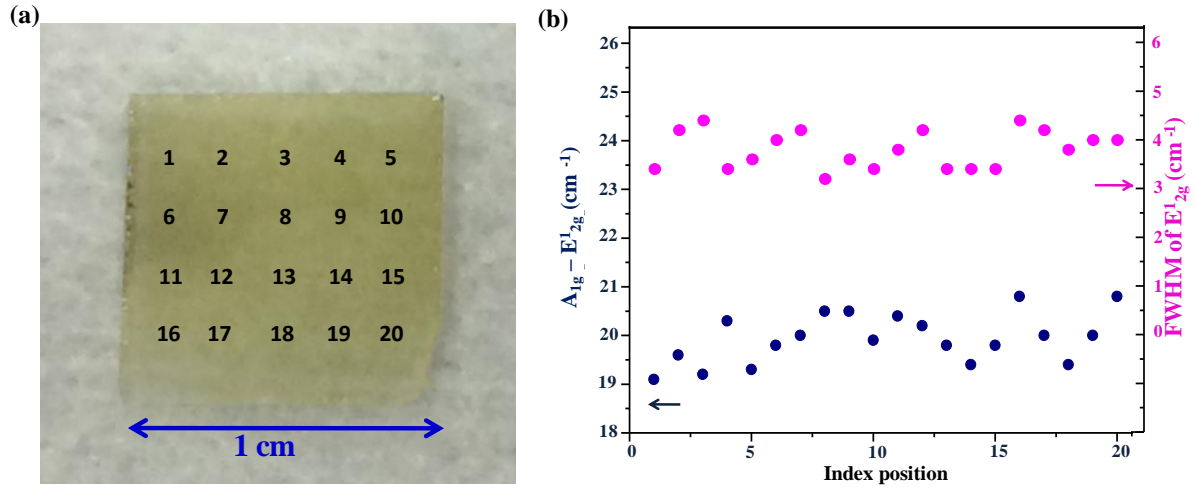


Fig. S8 Large-area, uniform single layer MoS₂. (a) Photograph of MoS₂ single layer grown on sapphire with numbers indicating sites of Raman statistical measurements. (b) Shows variation of difference (A_{1g} peak and E_{2g}^1 peak) and FWHM of E_{2g}^1 peak as a function of numbers indexed on the substrate.

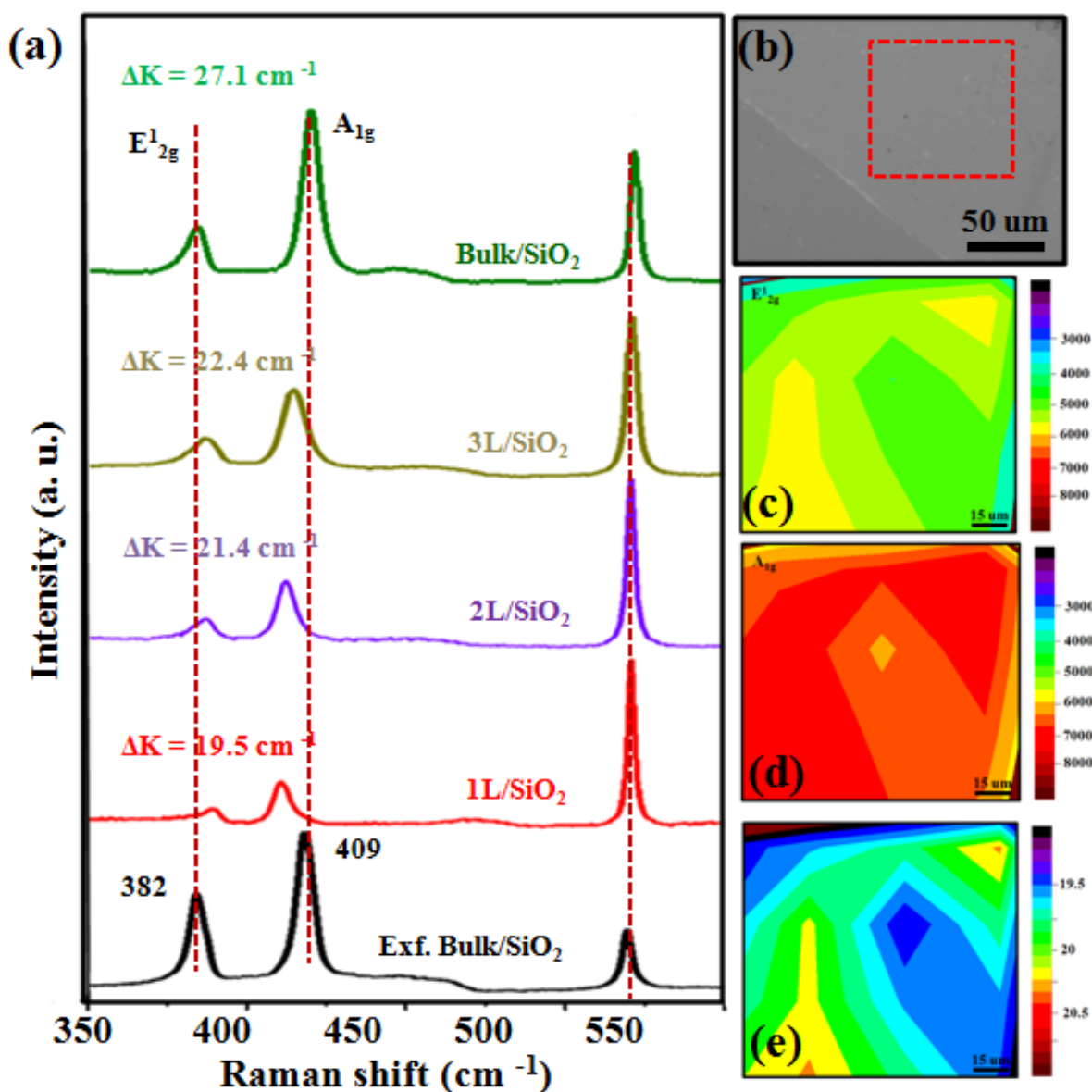


Fig. S9 (a) Raman spectra of MoS₂ layers (of different L) on SiO₂/Si. The spectrum of exfoliated bulk MoS₂ on SiO₂/Si is shown for comparison (b) Optical image of single layer of MoS₂ grown on SiO₂/Si, with a 100 μ m x 100 μ m area selected (c) Intensity mapping of the E₁_{2g} mode (d) Intensity mapping of the A_{1g} mode and (e) peak difference map.

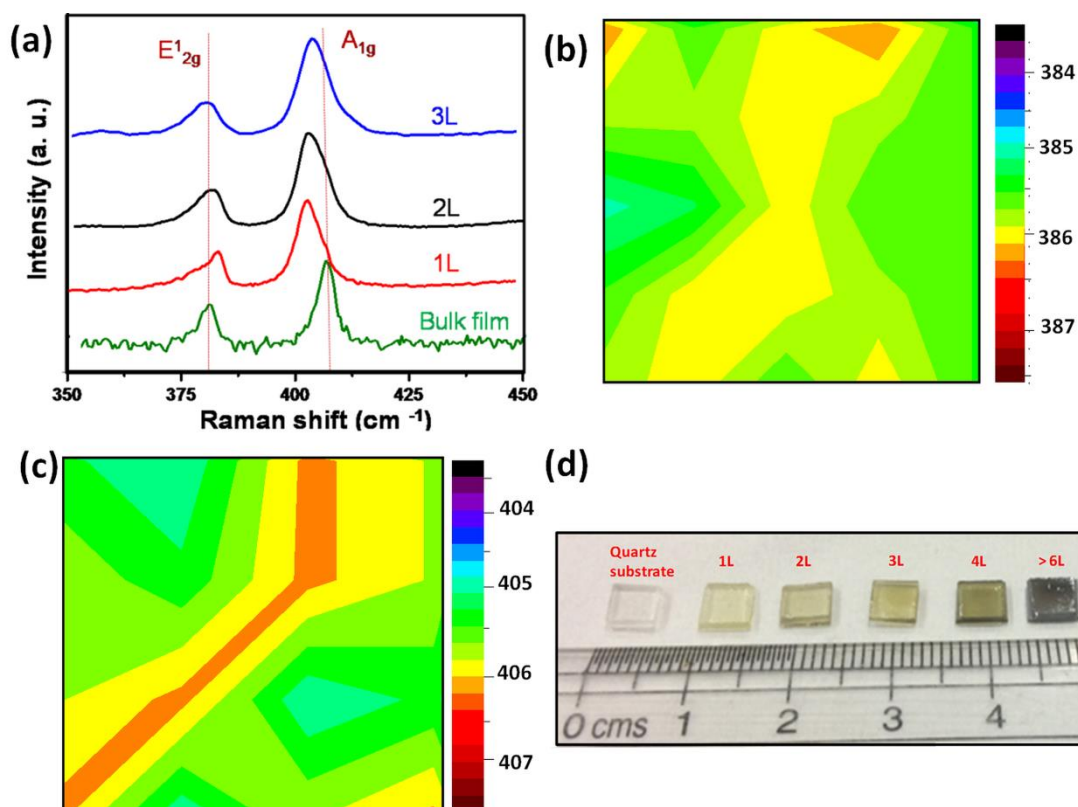


Fig. S10 (a) Raman spectra of MoS₂ layers (of different L) on quartz substrate. (b) monolayer Raman mapping for (b) the E_{12g} peak frequency (c) the A_{1g} peak frequency over a 15 μm × 15 μm scan area (d) Photograph of quartz substrates with different MoS₂ layers.

XPS data accuracy calibration-

The XPS scans were taken with an analyzer pass energy of 10 eV. Under these conditions, the actual chemical state could be identified from the peaks. The actual chemical state is necessary for accurate Mo:S ratio measurement. At the pass energy of 10 eV the signal to noise ratio is usually not very good. In order to increase this ratio, the scan was repeated 5 times. Increasing the number of scans further did not increase the signal to noise ratio. All the scans in the manuscript are ones with the highest obtained signal to noise ratio. In addition, the ratios calculated were obtained from 12 samples (5-3L, 5-4L and 2-5L). The ratio uniformity in the same sample was also measured over 3 spots. The error of ± 0.08 over this sample size makes us believe the accuracy of the XPS results.

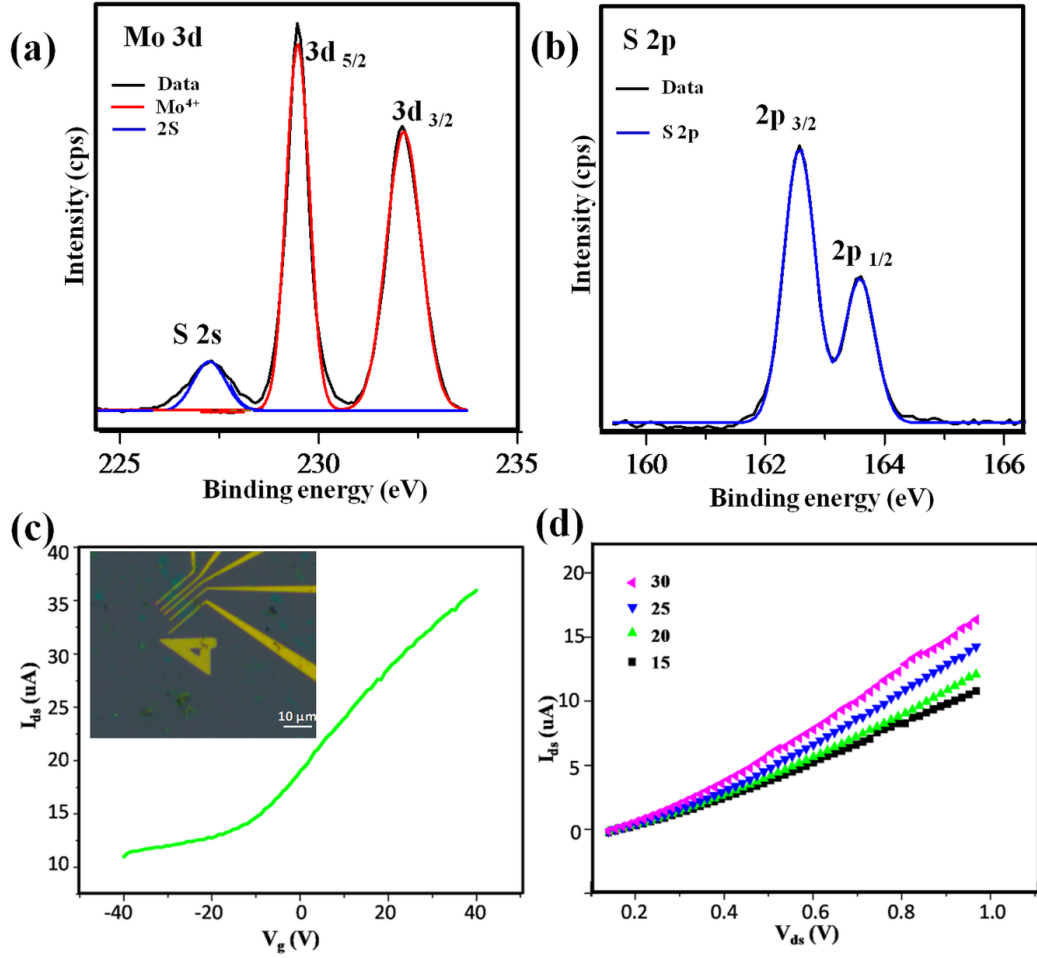


Fig. S11 (a) XPS spectra of exfoliated bulk MoS₂ on a Si/SiO₂ substrate for molybdenum (b) sulphur (c) Electrical properties of devices made on a bulk exfoliated MoS₂ flake. I_{ds}–V_{gs} curves for the bulk exfoliated MoS₂ FET shown in the inset is the optical image of the fabricated device. The FET carrier mobility extracted with channel L, W = 10 μm is 5.9 cm²/V-s at V_{ds} = 4V. (d) I_{ds}–V_{ds} curves for the device with varied back gate voltage V_{gs} at steps of 5 V.

Table S3: XPS data for exfoliated bulk MoS₂ and CVD grown p-type MoS₂

MoS ₂	Element	Area	Area/S _i	Atomic percentage	Atomic Ratio
CVD grown (Fig. 5d)	Mo 3d	3641	1324	0.292	0.8
	S 2s	1059	3209	0.702	2
Bulk exfoliated (Fig. S11)	Mo 3d	9164	3332	0.343	1
	S 2s	2099	6361	0.656	1.912

Carrier density determination

The sheet resistance, carrier concentration and the mobility of the MoS₂ films (3L and 5 nm films) were analyzed by using a Hall sensor measurement based on the Van der Pauw method.¹² All of the samples were with the same size (1 cm x 1 cm) with Cr/Au contacts which is expected to give an Ohmic contact to MoS₂. The results of measurements are listed in table S4.

Table S4. Results obtained from Hall measurements

	Hall measurement
Sheet resistance (kΩ/sq.)	989
Carrier concentration (cm ⁻³)	3 x 10 ¹⁶
Hall mobility (cm²/V-s)	44

Field-effect mobility measured earlier neglects the contact resistance and underestimates the mobility. From the Hall-effect measurements we show that mobility in 3L MoS₂ was underestimated by field effect measurement by a factor of 18.3.

We have also performed some simple calculations to show that the acceptor levels introduced by the defects expected justify the carrier levels measured as follows:

Calculation for carrier levels based on defect levels:

Total number of Mo atoms per unit volume in the MoS₂ crystal (n_{Mo})

$$n_{\text{Mo}} = \frac{\text{Density} \times N_A}{\text{Mol. Weight}}$$

$$n_{\text{Mo}} = \frac{(5.06 \text{ g cm}^{-3}) \times (6.023 \times 10^{23} \text{ mol}^{-1})}{(160.07 \text{ g mol}^{-1})}$$

$$n_{\text{Mo}} = 1.9 \times 10^{22} \text{ cm}^{-3}$$

From XPS data Mo ratio is 0.8, number of Mo vacancies (n_{VMo})

$$n_{VMo} = 0.2 \times 1.9 \times 10^{22} \text{ cm}^{-3} = 3.7 \times 10^{21} \text{ cm}^{-3}$$

From Hall measurements

$$\text{Carrier concentration (no. of holes)} = 3 \times 10^{16} \text{ cm}^{-3}$$

$$N_a = n_i (e^{((E_i - E_f)/KT)}) \quad (n_i = 1.6 \times 10^8 \text{ cm}^{-3})$$

$$E_i - E_f = 0.495 \text{ eV}$$

$$N_a^+ = \frac{N_a}{1 + g_A e^{((E_A - E_f)/KT)}}$$

$$3 \times 10^{16} = \frac{3.7 \times 10^{21}}{1 + 16(e^{((E_A - E_f)/KT)})} \quad g_A = 16 \text{ (i.e., } 4 \times 2 \times 2, \text{ Each } V_{Mo} \text{ can generate up to } 4 h^+, 2 \text{ spin and 2 V.B degeneracy)}$$

$$E_A - E_f = 0.23 \text{ eV}$$

$$E_g = 1.78 \text{ eV}$$

$$E_A - E_v = 0.62 \text{ eV}$$

This shows that the acceptor level introduced by the defect lies at 0.62 eV above the valence band edge in MoS₂. In Ref: 13 it has been shown point defects

References

- 1 G. Eriksson, *Acta Chemica Scandinavica*, 1971, **25**, 2651-2658.
- 2 A. Claudel, E. Blanquet, D. Chaussende, M. Audier, L. D. Pique and M. Pons, *Jornal of Crystal Growth*, 2009, **311**, 3371-3379.
- 3 S.Y. Kang, K.H. Choi, S.K. Lee, C.S. Hwang and H.J. Kim, *Journal of The Electrochemical Society*, 2000, **147**, 1161-1167.
- 4 S. Mukhopadhyay, K. Shalini, R. Lakshmi, A. Devi and S.A. Shivashankar, *Surface & Coatings Technology*, 2002, **150**, 205-211.
- 5 W.Y. Lee, T.M. Besmann and M.W. Stott, *Journal of Materials Research*, 1994, **9**, 1474-1483.
- 6 I. Endler, A. Leonhardt, U. Konig, H. van den Berg, W. Pitschke and V. Sottke, *Surface and Coatings Technology*, 1999, **120**, 482-488.
- 7 G. Di Giuseppe and J.R. Selman, *Journal of Electroanalytical Chemistry*, 2003, **559**, 31-43.
- 8 S. Dhar, A. Varade and S. A. Shivashankar, *Bulletin of Materials Science*, 2011, **34**, 11-18.
- 9 JANAF Thermochemical Tables : Parts I and II , 3rd edi., *J. Phycial and Chemical Reference Data*, **1985** ,14.
- 10 I. Barin , *Thermochemical Data of pure substances: Parts I and II*, 1989.
- 11 S. Wu, C. Huang, G. Aivazian, J. S. Ross, D. H. Cobden and X. Xu, *ACS Nano*, 2013, **7**, 2768-2772.
- 12 C. T. Lin, P. T. K. Loan, T.Y. Chen, K.K. Liu, C. H. Chen, K. H. Wei, *Adv. Func. Mater.*, 2013, **23**, 2301-2307.
- 13 J. F. Noh, H. Kim, Y. S. Kim, *Phys. Rev. B*, 2014, **89**, 205417.